J. Appl. Comput. Mech., 11(3) (2025) 754-769
DOI: 10.22055/jacm.2024.47772.4788

ISSN: 2383-4536
jacm.scu.ac.ir

Shahid Chamran University of Ahvaz

Journal of Applied and Computational Mechanics

Research Paper

Numerical Study of the Effects of the Navier Slip Boundary Condition on the Hydrodynamic Performances of a Newtonian Fluid-lubricated Pad Bearing

Ihssane Messoude[1], Samir Aghzer[1,2]

[1] Laboratory of Mechanics, Engineering and Innovation, National Higher School of Electricity and Mechanics, Hassan II University of Casablanca, Morocco,
Email: ihssane.messoude.doc21@ensem.ac.ma (I.M.); arzrsam365@gmail.com (S.A.)

[2] Higher School of Technology, Hassan II University of Casablanca, Morocco

Received August 19 2024; Revised October 16 2024; Accepted for publication October 30 2024.
Corresponding author: I. Messoude (ihssane.messoude.doc21@ensem.ac.ma)

Abstract. This study investigates the impact of the slip boundary condition at the Fluid/Solid interface on the hydrodynamic behavior of a pad bearing through a comprehensive numerical simulation. A modified Reynolds equation, derived from the Navier-Stokes equations and incorporating the Navier-type boundary conditions on the velocity field at wall contacts, was developed to model the system. The discretization of this equation was performed using the centered finite difference method where the resulting linear system of equations was numerically processed with the Gauss-Seidel iterative method enhanced by over-relaxation. The simulation reveals that introducing the slip condition allows the pad bearing to support loads even in configurations with divergent or parallel surfaces, a capability absent in conventional pad bearings. Specifically, for a convergence ratio of (1.5) and a slip zone covering (55%) of the upper surface, the pad bearing achieves a load capacity increase of (33.5%) compared to the conventional type. Furthermore, this non-conventional pad bearing reduces friction forces by up to (30%), enhancing performance while minimizing shear power dissipation. These numerical findings suggest that incorporating the slip boundary condition can significantly enhance both load capacity and efficiency in pad bearing applications.

Keywords: Hydrodynamic lubrication, Pad bearing, Navier slip boundary condition, Reynolds equation, Slip coefficient, Critical shear stress.

1. Introduction

Tribological applications generally extend to industrial machines where hydrodynamic journal and thrust bearings are frequently employed to bear and guide large shafts. The lubrication of these bearings relies on a fluid film that creates a separation between the contacting surfaces. This fluid film's hydrodynamic behavior is mathematically modeled by the Reynolds equation and is primarily affected by the flow's boundary conditions at the Fluid/Solid interface. In tribology, the no-slip boundary condition, which reflects the adhesion of the fluid to the solid walls, is commonly used [1]. However, studies reveal that the use of specially modified surfaces, such as hydrophobic surfaces, challenges this adhesion condition. Indeed, this property of hydrophobicity, or even super-hydrophobicity, significantly affects the kinematic behavior of the fluid, and partial slip is observed near the solid walls. This feature, often known as the lotus effect, generates considerable interest due to its many applications and benefits in various industrial sectors. For instance, superhydrophobic surfaces' property is particularly interesting in reducing aerodynamic or hydrodynamic drag [2].

The occurrence of slip at the Fluid/Solid interface was explored by Navier [3] and Maxwell [4] who suggested substituting the no-slip condition with a more general one. This new condition states that the fluid velocity at the wall is proportional to the fluid velocity gradient perpendicular to the wall, where the slip length (Navier length) serves as the proportionality constant. For a Newtonian fluid, this Navier condition translates to a proportionality between the fluid velocity at the wall and the shear stress at that wall. For a Newtonian fluid with threshold stress (critical shear stress), the Navier condition indicates that slip will take place at the Fluid/Solid interface whenever this threshold wall shear stress is surpassed. In order to characterize the slip phenomenon at a Fluid/Solid interface, scientists use two main parameters: the slip length and the slip velocity. Using techniques such as velocimetry which allows the visualization of fluid velocity profiles near a wall, experimental studies [5-9] have enabled precise measurements of slip lengths. Depending on the fluid properties, the flow geometry, the surface roughness, and the degree of surface hydrophobicity, the observed slip lengths vary from tens to hundreds of nanometers. In the case of lubrication oil flow in

Published online: November 06 2024

a hydrodynamic regime, experimental research by Pit et al. [10] and Henry et al [11] showed that wall slip occurs even for a Newtonian fluid.

To study the introduction of the slip property in tribology, previous research has been conducted on various types of hydrodynamic contacts. Among these contacts are the pad bearing, which consists of two converging contact surfaces-one generally stationary and the other movable-and the journal bearing, where the contact surfaces are cylindrical, with one surface typically stationary (the housing) and the other movable (the shaft). When the slip condition is partially or fully imposed on one of the contact surfaces, a change in hydrodynamic behavior is observed. In these previous studies, the main objective has been to assess the impact of the Navier slip condition on the bearing's load capacity and efficiency. In the case of a pad bearing where the stationary surface is fully subjected to the slip condition, Spikes et al. [12,13] evaluated how the critical shear stress affects both the frictional force and the load capacity. They showed that "half-wetted" contacts generate significant load support with low friction. Salant and Fortier [14] indicated that using a heterogeneous sliding/non-sliding surface can enhance the pad bearing's load capacity while reducing friction. Through numerical analysis of the impact of the slip region extent on the fixed surface of a pad bearing, Wu et al. [15] showed that the maximum load gain is achieved with convergence ratio values slightly exceeding unity. On the other hand, the authors demonstrated that the pad bearing still has load capacity even with divergent or parallel-surface contact. Furthermore, Wu [16] showed that incorporating a slip region on a journal bearing's housing surface significantly improves its performance. The results indicate that this type of bearing offers several advantages over conventional journal bearings, including a substantial increase in load support, which is enhanced by 19%. This numerical study presents an approach for designing an optimized slip region not only for journal bearings but also for thrust bearings, and it shows that the slip region location and size significantly impact the bearing's performance. Rao [17] proposed a theoretical model to examine the slip condition applied to the stationary surface in converging contacts as well as journal bearings. For a pad bearing, the results show that the pressure distribution is more substantial than in the conventional case. More than that, this distribution is not affected by an increase in the slip coefficient beyond a certain threshold. When considering flow between two infinitely long parallel surfaces, with the stationary surface partially subjected to the slip condition, Lin et al. [18] investigated the impact of the slip region position and extent on the frictional force and the load capacity. They have indicated that the frictional force is solely dependent on the slip region length, while the load capacity also depends on its location (start and end of the region). In the case of lubricated converging contacts, whether one-dimensional [19] or two-dimensional [20], Tauviqirrahman et al. demonstrated the advantages of the slip property when applied to one of the contact surfaces to produce substantial hydrodynamic pressure and minimal frictional force. They indicated that it is crucial to carefully choose slip parameters to enhance performances, showing that the optimized lubricated contact should incorporate a diminished critical shear stress associated with a large slip zone length. Moreover, Zidane et al. [21] examined a two-dimensional pad bearing in which the stationary surface is fully affected by the slip condition. Their results show that this slip property reduces friction by using a low critical shear stress but does not improve the pad bearing's load capacity, as it has been demonstrated to be maximal in the conventional case (in the absence of slip). Experimental tests were conducted by Guo et al. [22] on a pad bearing to study the influence of sliding speed and lubricant viscosity. The results from the experimental measurements of the lubricant film thickness indicate that all measured values were lower than the theoretical values without slip, a phenomenon attributed to the reduction in adhesion at the Fluid/Solid interface, resulting either from the application of a hydrophobic coating or from the incorporation of additives in the lubricant. Using a numerical analysis validated by experimental tests on two sliding patterns (central stripe and inverse triangle) located on the stationary surface of a two-dimensional lubricated contact, the results of Sun et al. [23] show that these patterns significantly enhance load capacity, particularly upon reaching a critical threshold shear of zero. Concerning a water-lubricated journal bearing, Xie et al. [24] demonstrated the impact of the Navier condition and inertial force on contact performance, confirming the accuracy of the Reynolds equation compared to simulations conducted with FLUENT software. The findings indicate that the water film pressure distribution, the load capacity, and the frictional force are not markedly altered under slip property and inertia effects. A novel model for simulating both wall slip and cavitation in two-dimensional hydrodynamic lubrication has been proposed by Çam et al. [25]. The study validates this model through tests on various bearing types, including journal and slider bearings, and shows that the tribological performance of hydrodynamic lubricated contacts is improved even in the presence of cavitation. Their findings also suggest that optimizing hydrophobic surfaces can enhance the performance, although manufacturing costs are a consideration. Besides, using the optimization method based on the genetic algorithm, Zhang et al. [26] sought the shape and extent of the slip contact zone that optimizes the performance of a two-dimensional pad bearing, whose moving surface is partially or fully subjected to the slip condition. The influence of contact width, convergence ratio, and slip coefficient was studied. Their results show that this zone always has the shape of a regular trapezoid, with the larger base located at the entry of the contact. Zhang and Zhu [27] investigated a two-dimensional pad bearing with a hydrophobic moving surface using the Monte Carlo optimization method. The optimal search for the slip contact zone was examined. Regarding the shape and position of the optimal slip zone, their findings are consistent with those of Zhang et al. [26]. The pad bearing's aspect ratio (ratio of length to width) impact was studied. In the case of single-objective optimization, which aims to maximize load capacity, the results show that the slip contact zone's area increases with the pad bearing's aspect ratio. In the case of multi-objective optimization, which aims to simultaneously maximize load capacity and minimize friction force (two conflicting objectives), the findings show that the load capacity decreases as the pad bearing's aspect ratio increases, while the friction force increases.

The simplest geometric configuration of a hydrodynamic bearing is the pad bearing. This type of bearing finds its application in hydrodynamic thrust bearings. Figure 1(a) shows a photographic representation of the rotational guidance of a vertical shaft using a fixed pad hydrodynamic thrust bearing. This hydrodynamic thrust bearing is part of an experimental test rig, according to [28]. The thrust pad, which directly supports the load, is stationary and, in this case, has eight fixed pads, as shown in Fig. 1(b). The runner, which has the shape of a smooth disk, is rotating.

This work centers on the numerical analysis of the hydrodynamic behavior of a pad bearing, whose upper surface is stationary and partially or fully subjected to the slip condition (non-conventional pad bearing). After a mathematical formulation aimed at developing the so-called modified Reynolds equation, which governs the hydrodynamic behavior of the pad bearing, as well as the literal expressions of its different performances, the next step involves the numerical calculation. According to the convergence ratio of the contact, the slip zone starting position and length, and the slip coefficient value, the hydrodynamic performances of such a contact are obtained and compared to those of the conventional pad bearing. The key novelty of this study lies in the graphical representations that offer clearer and more insightful visualizations of how introducing slip can significantly alter the hydrodynamic behavior of a pad bearing, including load capacity, pressure distribution, shear power dissipation, and volumetric flow rate. This not only revises the theoretical model but also enhances the practical understanding of pad bearings, especially for applications requiring precise and efficient bearing systems.

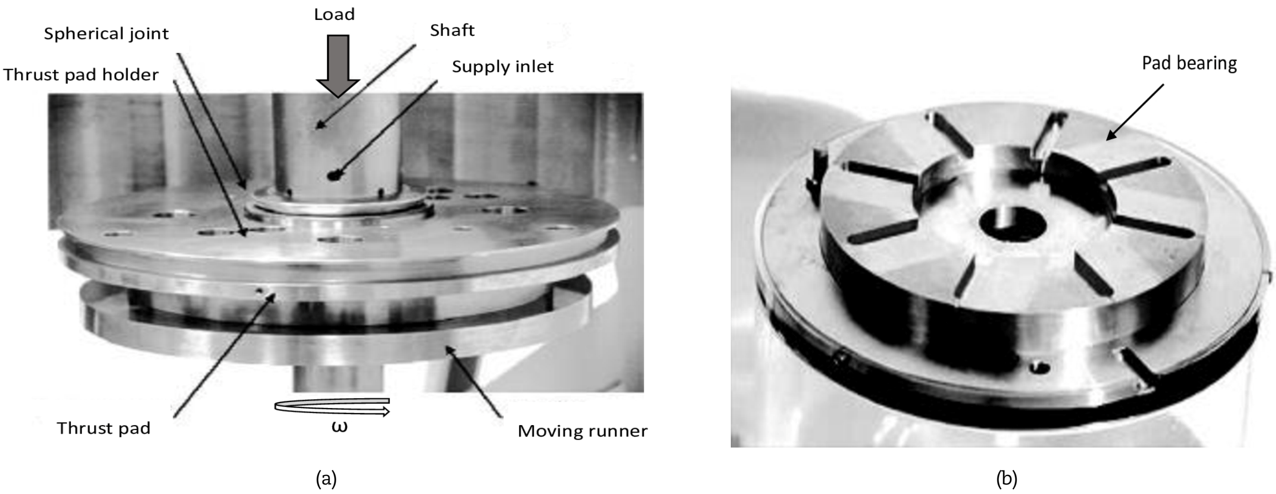

Fig. 1. (a) Rotational guidance of a shaft by a fixed pad hydrodynamic thrust bearing [28], (b) Thrust bearing with 8 fixed pads [28].

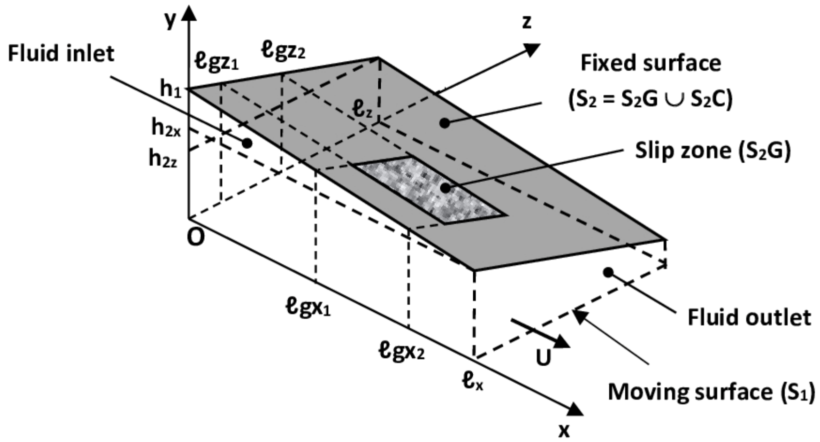

Fig. 2. Two-dimensional schematic of a pad bearing.

2. Mathematical Modeling

This section presents the modified Reynolds equation governing the hydrodynamic behavior of a non-conventional pad bearing (Fig. 2), where the slip condition is assumed partially or fully on the fixed upper surface (S_2) over a rectangular zone (S_2G) aligned parallel to the (x) and (z) directions with lengths ($\ell gx = (\ell gx_2 - \ell gx_1)$) and ($\ell gz = (\ell gz_2 - \ell gz_1)$). Elsewhere on the rest of the surface (S_2), the fluid adheres to the wall. The lower surface (S_1), moving with a uniform translation velocity (U), is conventional.

2.1. Slip-adhesion condition

To determine the velocity field of a moving fluid, its flow description must account for boundary conditions that reflect its behavior at the wall. The no-slip (adhesion) condition, assuming the fluid's velocity relative to the wall to be zero, is commonly adopted. However, this condition is an idealization of reality. Navier [3] and Maxwell [4] proposed substituting the no-slip condition with a more general condition which, in our case, can be expressed as:

$$u_p = \pm b\left(\frac{\partial u}{\partial y}\right)_{y=h} \tag{1}$$

(u_p) is the fluid velocity at the wall and (b) is the slip length (Navier length).
(α) and (μ) are, respectively, the slip coefficient and the dynamic fluid viscosity where; $b = \alpha\mu$.
($y = h$) represents the Fluid/Solid interface at the fixed surface (S_2).

This condition assumes a direct relationship between the fluid velocity at the wall and the fluid velocity gradient at the wall. A schematic interpretation for this boundary condition is depicted in Fig. 3 [3, 7, 8]. Case (a) corresponds to a no-slip condition (full adhesion), which results in a zero-slip length. Case (b) corresponds to partial slip through a finite slip length. Finally, case (c) represents perfect slip, resulting in an infinitely large slip length.

More generally, the slip condition reflects the equality between the stress and the friction that the solid wall imparts to the fluid through the slip coefficient:

$$u_p = \mp\alpha\tau_p \tag{2}$$

The wall shear stress for a Newtonian fluid is expressed as:

$$\tau_p = \mu\left(\frac{\partial u}{\partial y}\right)_{y=h} \tag{3}$$

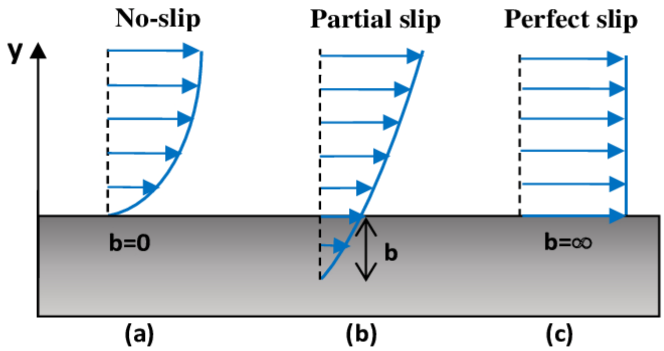

Fig. 3. Slip length configurations.

In the presence of the slip condition, the wall shear stress τ_p can exhibit a critical stress threshold τ_c (critical shear stress) and is then expressed as:

$$\tau_p = \mu\left(\frac{\partial u}{\partial y}\right)_{y=h} + \tau_c \tag{4}$$

Finally, taking into account Eq. (1) to Eq. (4), the slip-adhesion conditions are written:

$$\begin{cases} u_p = 0; & \tau_p < \tau_c \\ u_p = \mp\alpha\left[\mu\left(\frac{\partial u}{\partial y}\right)_{y=h} + \tau_c\right]; & \tau_p \geq \tau_c \end{cases} \tag{5}$$

These boundary conditions are reduced to the Navier conditions Eq. (1) with a critical shear stress of zero, where the slip velocity varies in proportion to the shear stress.

2.2. Modified Reynolds equation

For steady laminar flow of an incompressible Newtonian isoviscous fluid, the Navier Stokes equations governing the fluid flow within the pad bearing are written as:

$$\begin{cases} \frac{\partial P}{\partial x} = \mu\frac{\partial^2 u}{\partial y^2} \\ \frac{\partial P}{\partial y} = 0 \\ \frac{\partial P}{\partial z} = \mu\frac{\partial^2 w}{\partial y^2} \end{cases} \tag{6}$$

Assuming the isotropy of both the slip coefficient and the critical shear stress, and considering the slip-adhesion boundary conditions Eq. (5) written at surfaces (S_1) and (S_2):

- Regarding surface (S_1):

$$\begin{cases} u(y=0) = U \\ w(y=0) = 0 \end{cases} \tag{7a}$$

- Regarding surface (S_2C):

$$\begin{cases} u(y=h) = 0 \\ w(y=h) = 0 \end{cases} \tag{7b}$$

- Regarding surface (S_2G):

$$\begin{cases} u(y=h) = 0; & \tau_{xy} < \tau_c \\ u(y=h) = -\alpha\left[\mu\left(\frac{\partial u}{\partial y}\right)_{y=h} + \tau_c\right]; & \tau_{xy} \geq \tau_c \\ w(y=h) = 0; & \tau_{yz} < \tau_c \\ w(y=h) = -\alpha\left[\mu\left(\frac{\partial w}{\partial y}\right)_{y=h} + \tau_c\right]; & \tau_{yz} \geq \tau_c \end{cases} \tag{7c}$$

The equations for the velocity fields (u) and (w), respectively in the (x) and (z) directions, are written as:

$$\begin{cases} u(y) = \frac{1}{2\mu}\frac{\partial P}{\partial x}y^2 - \frac{h}{2\mu}\frac{\partial P}{\partial x}\left(1 + \frac{\alpha\mu}{h+\alpha\mu}\right)y - \frac{\alpha\tau_c}{h+\alpha\mu}y - \frac{U}{h+\alpha\mu}y + U \\ w(y) = \frac{1}{2\mu}\frac{\partial P}{\partial z}y^2 - \frac{h}{2\mu}\frac{\partial P}{\partial z}\left(1 + \frac{\alpha\mu}{h+\alpha\mu}\right)y - \frac{\alpha\tau_c}{h+\alpha\mu}y \end{cases} \tag{8}$$

The modified dimensional Reynolds equation in Eq. (9), which is based on the mass conservation equation, is then written as:

$$\begin{aligned}&\frac{\partial}{\partial x}\left[\frac{-h^3}{12\mu}\frac{\partial P}{\partial x}\left(1+\frac{3\alpha\mu}{h+\alpha\mu}\right)\right]+\frac{\partial}{\partial z}\left[\frac{-h^3}{12\mu}\frac{\partial P}{\partial z}\left(1+\frac{3\alpha\mu}{h+\alpha\mu}\right)\right]+\alpha\mu\left[\frac{h}{2\mu}\frac{\partial P}{\partial x}\left(1-\frac{\alpha\mu}{h+\alpha\mu}\right)\right]\frac{\partial h}{\partial x}\\&+\alpha\mu\left[\frac{h}{2\mu}\frac{\partial P}{\partial z}\left(1-\frac{\alpha\mu}{h+\alpha\mu}\right)\right]\frac{\partial h}{\partial z}-\frac{\partial}{\partial x}\left[\frac{h^2}{2}\frac{U}{h+\alpha\mu}+\frac{h^2}{2}\frac{\alpha\tau_c}{h+\alpha\mu}-Uh\right]-\frac{\partial}{\partial z}\left[\frac{h^2}{2}\frac{\alpha\tau_c}{h+\alpha\mu}\right]\\&-\alpha\mu\left[\frac{U}{h+\alpha\mu}+\frac{\alpha\tau_c}{h+\alpha\mu}-\frac{\tau_c}{\mu}\right]\frac{\partial h}{\partial x}-\alpha\mu\left[\frac{\alpha\tau_c}{h+\alpha\mu}-\frac{\tau_c}{\mu}\right]\frac{\partial h}{\partial z}=0\end{aligned}\tag{9}$$

For a slip coefficient of zero $(\alpha=0)$, the classical Reynolds equation for a conventional pad bearing is recovered [1]. Considering the various dimensionless parameters adopted (see Nomenclature), the expressions for the dimensionless velocity fields $(\bar{u})$ and $(\bar{w})$ are expressed as:

$$\begin{cases}\bar{u}(\bar{y})=\dfrac{1}{2}\dfrac{\partial\bar{P}}{\partial\bar{x}}\left[\bar{y}-\dfrac{H(H+2A)}{H+A}\right]\bar{y}-\dfrac{A\bar{\tau}_c+1}{H+A}\bar{y}+1\\ \bar{w}(\bar{y})=\dfrac{L}{2}\dfrac{\partial\bar{P}}{\partial\bar{z}}\left[\bar{y}-\dfrac{H(H+2A)}{H+A}\right]\bar{y}-\dfrac{A\bar{\tau}_c}{H+A}\bar{y}\end{cases}\tag{10}$$

Finally, the modified dimensionless Reynolds equation can be written as:

$$\begin{aligned}&H(H+4A)\frac{\partial^2\bar{P}}{\partial\bar{x}^2}+L^2H(H+4A)\frac{\partial^2\bar{P}}{\partial\bar{z}^2}+\frac{3}{(H+A)}\left[(H+A)^2+A^2\right]\frac{\partial H}{\partial\bar{x}}\frac{\partial\bar{P}}{\partial\bar{x}}\\&+\frac{3L^2}{(H+A)}\left[(H+A)^2+A^2\right]\frac{\partial H}{\partial\bar{z}}\frac{\partial\bar{P}}{\partial\bar{z}}+\frac{3H^2}{(H+A)}\frac{\partial A}{\partial\bar{x}}\frac{\partial\bar{P}}{\partial\bar{x}}+\frac{3L^2H^2}{(H+A)}\frac{\partial A}{\partial\bar{z}}\frac{\partial\bar{P}}{\partial\bar{z}}\\&-\frac{6(1+A\bar{\tau}_c)}{(H+A)}\frac{\partial H}{\partial\bar{x}}-\frac{6LA\bar{\tau}_c}{(H+A)}\frac{\partial H}{\partial\bar{z}}+\frac{6(\bar{\tau}_cH-1)}{(H+A)}\frac{\partial A}{\partial\bar{x}}+\frac{6L\bar{\tau}_cH}{(H+A)}\frac{\partial A}{\partial\bar{z}}=0\end{aligned}\tag{11}$$

In this equation, $\bar{P}(\bar{x},\bar{z})$, $H(\bar{x},\bar{z})$, and $A(\bar{x},\bar{z})$ represent the dimensionless fields of pressure, film thickness, and slip within the contact, respectively.

Solving Eq. (11) allows to determine the dimensionless pressure field within the contact. To achieve this, knowledge of the boundary conditions on the pressure field is essential. These boundary conditions largely depend on the fluid supply mode of the hydrodynamic contact [1]. In this case, it is assumed that the bearing is submerged in a fluid bath. Therefore, the pressures at the edges of the pad bearing are equal to the ambient atmospheric pressure, which is assumed to be zero.

Thus, the boundary conditions considered on the pressure field can be expressed as:

$$\bar{P}(0,\bar{z})=\bar{P}(1,\bar{z})=\bar{P}(\bar{x},0)=\bar{P}(\bar{x},1)=0 \qquad 0\le\bar{x}\le1\ ;\ 0\le\bar{z}\le1\tag{12}$$

With this field, all hydrodynamic performances of the pad bearing can be obtained. Specifically, these include the load capacity, the friction force due to shear dissipation, particularly at the lower moving surface, and the volumetric flow rate required for hydrodynamic lubrication.

2.3. Evaluation of the pad bearing's performances

Knowing the pressure field, the dimensionless load capacity $(\bar{W})$, defined as the integral of the pressure field within the contact, is written as:

$$\bar{W}=\int_0^1\int_0^1\bar{P}d\bar{x}d\bar{z}\tag{13}$$

By integrating the shear stresses (τ_{xy}) and (τ_{yz}) over the lower surface of the contact (S_1), the dimensionless friction forces $(\bar{F}_x)$ and $(\bar{F}_z)$ acting in the (x) and (z) directions, respectively, on the lower surface (S_1), are expressed as:

$$\begin{aligned}\bar{F}_x&=-\int_0^1\int_0^1\left[\frac{H(H+2A)}{2(H+A)}\frac{\partial\bar{P}}{\partial\bar{x}}+\frac{1}{(H+A)}+\frac{A\bar{\tau}_c}{(H+A)}\right]d\bar{x}d\bar{z}\\ \bar{F}_z&=-\int_0^1\int_0^1\left[\frac{LH(H+2A)}{2(H+A)}\frac{\partial\bar{P}}{\partial\bar{z}}+\frac{A\bar{\tau}_c}{(H+A)}\right]d\bar{x}d\bar{z}\end{aligned}\tag{14}$$

The dimensionless flow rates $(\bar{Q}_x)$ and $(\bar{Q}_z)$, respectively, in the (x) and (z) directions, are calculated as the fluxes of the velocity fields $(\bar{u})$ and $(\bar{w})$:

$$\begin{aligned}\bar{Q}_x&=\int_0^1\left[-\frac{H^3}{4}\left(\frac{1}{3}+\frac{A}{(H+A)}\right)\frac{\partial\bar{P}}{\partial\bar{x}}-\frac{H^2(1+A\bar{\tau}_c)}{2(H+A)}+H\right]d\bar{z}\\ \bar{Q}_z&=-\int_0^1\left[\frac{LH^3}{4}\left(\frac{1}{3}+\frac{A}{(H+A)}\right)\frac{\partial\bar{P}}{\partial\bar{z}}+\frac{A\bar{\tau}_cH^2}{2(H+A)}\right]d\bar{x}\end{aligned}\tag{15}$$

3. Numerical Resolution

The modified Reynolds equation in Eq. (11) is a two-dimensional, second-order partial differential equation. It lacks an analytical solution. The adopted numerical solution is the centered finite difference method. This widely used method in hydrodynamic lubrication allows for sufficient accuracy in solving most hydrodynamic problems.

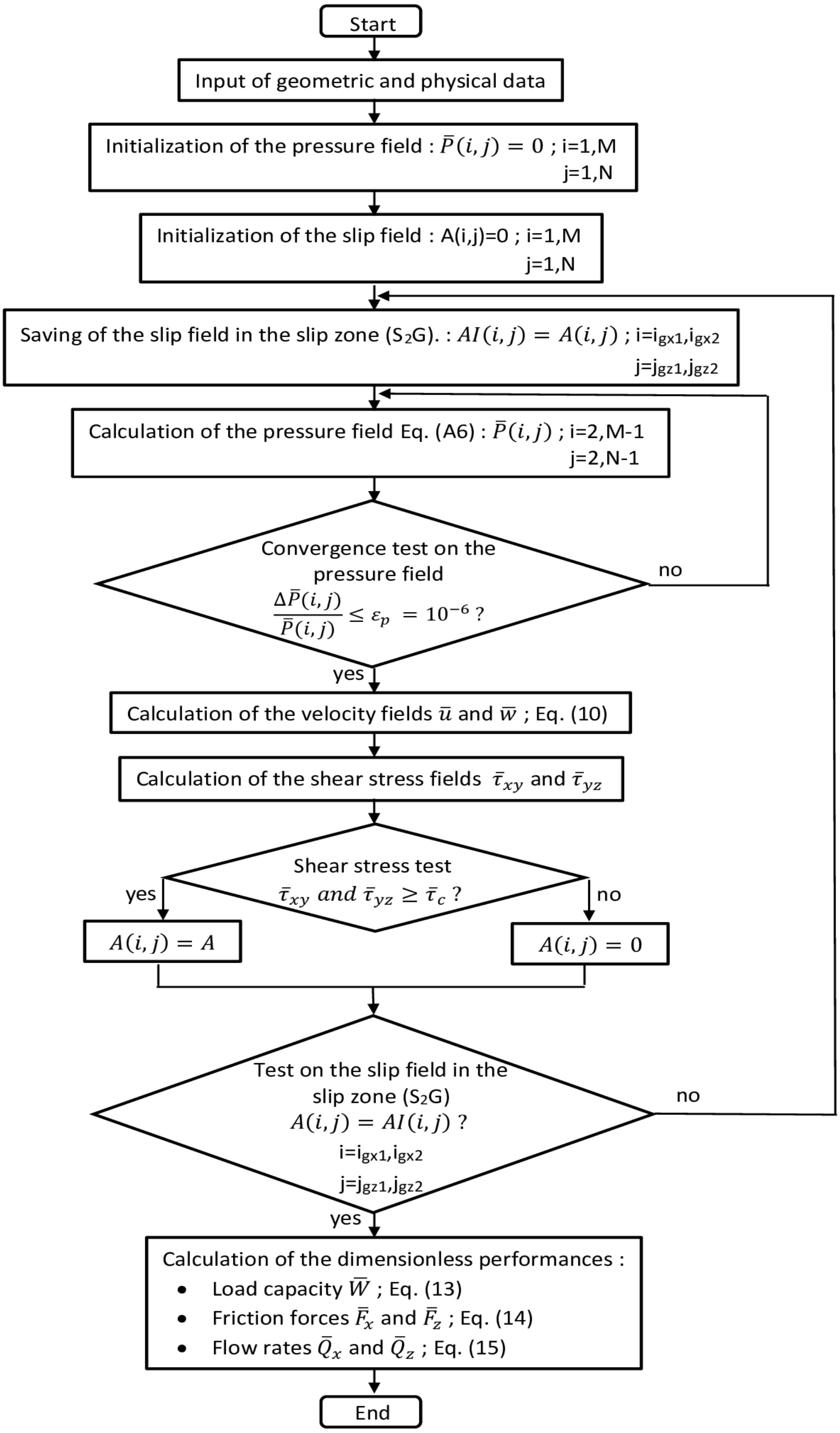

Fig. 4. Flow chart of the calculation process.

The rectangular domain of the surface (S_1) ($\Omega = \ell_x * \ell_z$) is discretized into a grid of (M*N) points. The resulting system of equations is iteratively solved using the Gauss-Seidel method with over-relaxation (see Appendix A).

The iterative resolution scheme adopted is represented by the flow chart in Fig. 4.

The pressure field calculation process stops when the relative numerical error in pressure is less than or equal to ($\varepsilon_p = 10^{-6}$). The slip field ($A(\bar{x},\bar{z})$) within the slip zone is determined based on the prevailing shear stress field. It is zero in conventional zones ((S_1) and (S_2C) surfaces) and takes on a specified value in the slip zone (S_2G).

Regarding the numerical calculation of the hydrodynamic performances of the pad bearing, it should be noted that the dimensionless load capacity ($\bar{W}$) Eq. (13) and the dimensionless friction forces ($\bar{F}_x$) and ($\bar{F}_z$) Eq. (14) are obtained using the rectangle method. Meanwhile, the dimensionless flow rates ($\bar{Q}_x$) and ($\bar{Q}_z$) Eq. (15) are obtained using the trapezoidal method.

Table 1. Computational time as a function of the mesh size.

Mesh (M*N)	CPU Time [s]
100*100	0.89
150*150	4.03
200*200	11.64
300*300	64.80

This algorithm is implemented as a calculation code using the Fortran programming language.

In the case of a conventional one-dimensional pad bearing operating under a steady laminar regime, the curves in Fig. 5(a), 5(b), and 5(c) represent the variations of the dimensionless load capacity ($\bar{W}$), friction force ($\bar{F}_x$), and flow rate ($\bar{Q}_x$) as a function of the convergence ratio (H_1). This is for different mesh finenesses (M*N) ranging from (100*100) to (300*300).

It is noted that these variations are, on the one hand, qualitatively and quantitatively in agreement with those of Frene et al. [1]. On the other hand, it is observed that starting from a mesh size (M*N = 100*100), the convergence and accuracy of the calculations are ensured. However, computational time increases with mesh size. Indeed, for a convergence ratio (H_1 = 1.5) and an accuracy of ($\varepsilon_p = 10^{-6}$) for the pressure field calculation, Table 1 illustrates the required computational times as a function of the mesh size. Therefore, the mesh size (M*N = 100*100), which provides both satisfactory accuracy and rapid convergence of the calculations, will be retained in the following.

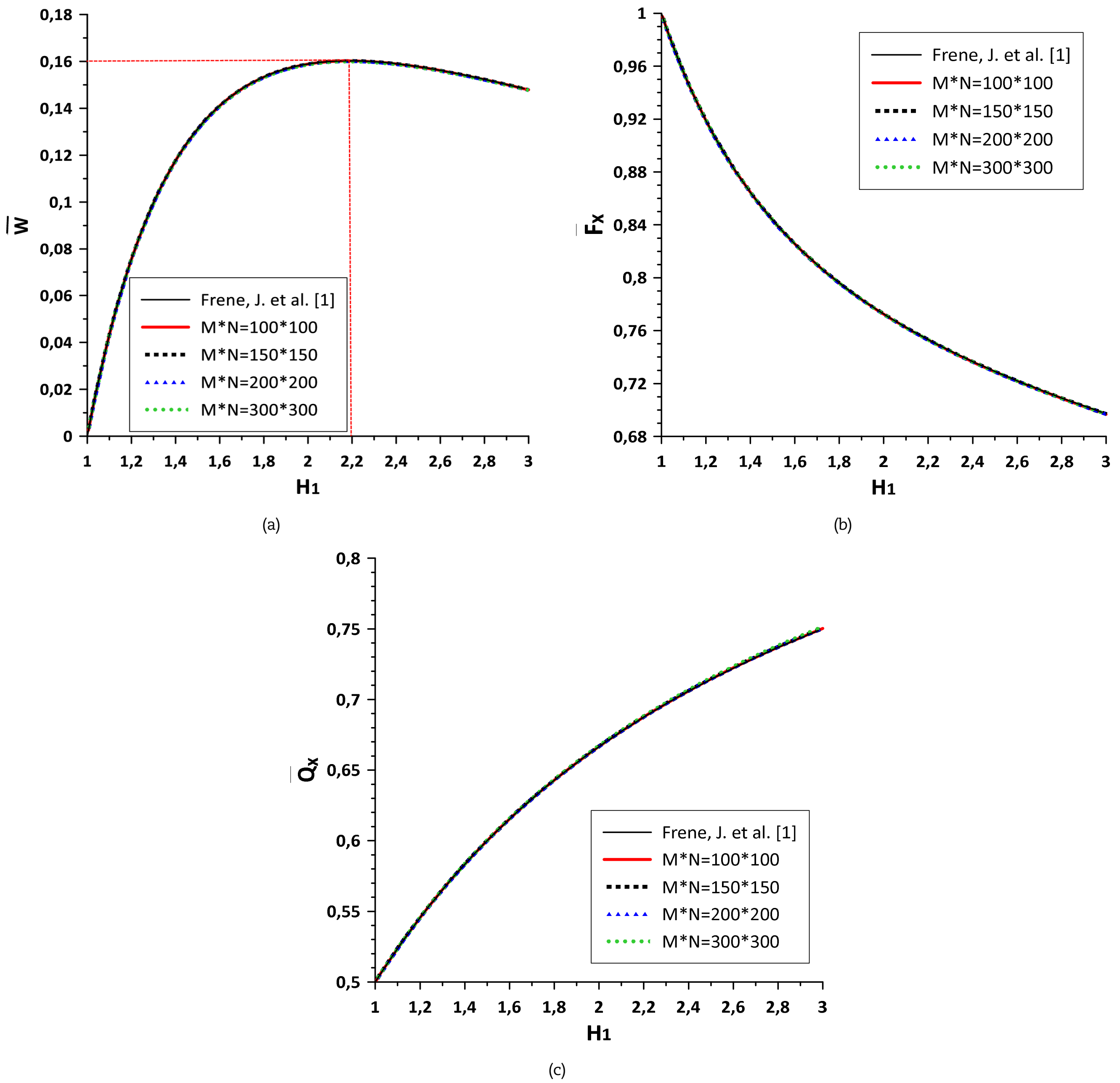

Fig. 5. (a) Variation of the dimensionless load capacity as a function of the convergence ratio for different finesses of the mesh, (b) Variation of the dimensionless friction force as a function of the convergence ratio for different finesses of the mesh, (c) Variation of the dimensionless flow rate as a function of the convergence ratio for different finesses of the mesh.

Table 2. Geometric and physical data.

ℓ_x	0.15 [m]
ℓ_z	1 [m]
h_{2x}	30×10^{-6} [m]
H_1	[0.5, 3]
U	75 [m/s]
μ	0.04 [Pa.s]

4. Results and Discussion

This section focuses on a numerical study examining the effects of the slip coefficient, the slip zone position and extent, and also the critical shear stress on the hydrodynamic performances of a pad bearing. Particularly, the analysis includes load capacity, pressure distribution, shear friction force dissipated on the moving surface, and fluid volumetric flow rate.

The numerical results pertain to a one-dimensional pad bearing (with infinite width ℓ_z), where the upper fixed surface (S_2) is partially or completely subjected to the slip condition over a dimensionless length zone ($\bar{\ell}_{gx}$); (Fig. 6).

The geometric and physical data for this study are presented in Table 2.

In this study, the ranges of variation adopted for the convergence ratio (H_1) in the case of the conventional and non-conventional pad bearing are [1.5, 3] and [0.5, 3], respectively. Indeed, these values ensure compliance with the aspect ratio (the ratio of the average film thickness to the contact length), which must be on the order of (10^{-3}) [1]. Additionally, these values guarantee a laminar flow regime within the hydrodynamic contact.

Depending on whether the critical shear stress is zero or not, two cases are investigated.

In the case of a conventional pad bearing, the maximum dimensionless values of pressure ($\bar{P}_{cmax}$) and load capacity ($\bar{W}_{cmax}$) are (0.260) and (0.160), respectively, for a convergence ratio of (2.2) [1].

4.1. Zero critical shear stress case ($\bar{\tau}_c = 0$)

For a slip zone length ($\bar{\ell}_{gx}$) of (50%) and convergence ratios (H_1) ranging from (1.5) to (3), Fig. 7 illustrates the evolution of the load capacity gain ($\bar{W}/\bar{W}_c$), which is the ratio of the load capacity of a pad bearing affected by the slip condition to that of a conventional pad bearing, for the same convergence ratio, as a function of the dimensionless slip coefficient (A).

On the one hand, it is noted that for any convergence ratio (H_1) ranging from (1.5) to (2.2), the load capacity gain increases until it reaches a maximum value, which corresponds to a value of the dimensionless slip coefficient (A) that is close to (1), after which it decreases monotonically. The maximum load capacity gain depends on the convergence ratio (H_1). For low values of the dimensionless slip coefficient ($0 < A < 3$), there is a substantial improvement in load capacity gain for convergence ratios H_1 ranging from (1.5) to (2.2). On the other hand, it is observed that for any given convergence ratio (H_1), there is a limit dimensionless slip coefficient value (A) above which there is no further gain in load capacity. For relatively large convergence ratios (H_1 = 2.5 and 3), it can be seen that there is no load capacity gain regardless of the slip coefficient value. Moreover, it is noted that, for the same slip coefficient, the load capacity gain varies inversely proportional to the convergence ratio (H_1). Finally, the maximum load capacity gain occurs at a convergence ratio of (H_1 = 1.5) and a dimensionless slip coefficient of (A=0.95). In this case, the non-conventional pad bearing provides a load capacity gain of (33.45%) compared to a conventional pad bearing with an identical convergence ratio.

For a dimensionless slip coefficient (A=0.95) and convergence ratios (H_1) ranging from (0.5) to (3), Fig. 8 illustrates the evolution of the optimum load capacity gain ($\bar{W}/\bar{W}_{cmax}$), relative to the maximum dimensionless load capacity of a conventional pad bearing ($\bar{W}_{cmax}$ = 0.160 for H_1 = 2.2), plotted against the dimensionless slip zone length ($\bar{\ell}_{gx}$).

Firstly, the pad bearing can support a load even with a convergence ratio less than or equal to (1), which is unachievable with a conventional pad bearing. Secondly, it is observed that for any convergence ratio (H_1) ranging from (0.5) to (3), the optimal load capacity gain increases until it reaches a maximum value, which corresponds to a limit value of the dimensionless slip zone length of (55%) or greater, after which it decreases sharply and monotonically. The maximum load capacity gain depends on the convergence ratio (H_1), and it occurs at a convergence ratio of (H_1 = 1.5) and a slip zone length ($\bar{\ell}_{gx}$) of (55%). In this case, the maximum dimensionless load capacity reaches (0.175), exceeding that of the optimal conventional pad bearing by (9.26%). These results align with those of Wu et al. [15]. Indeed, they show that for zero critical shear stress case, the maximum load capacity is achieved when the pad bearing surfaces are nearly parallel ($H_1 \approx 0.9$), with a slip zone length of (65%). Additionally, it is noted that for slip zone lengths above (70%), the load capacity decreases significantly regardless of the convergence ratio.

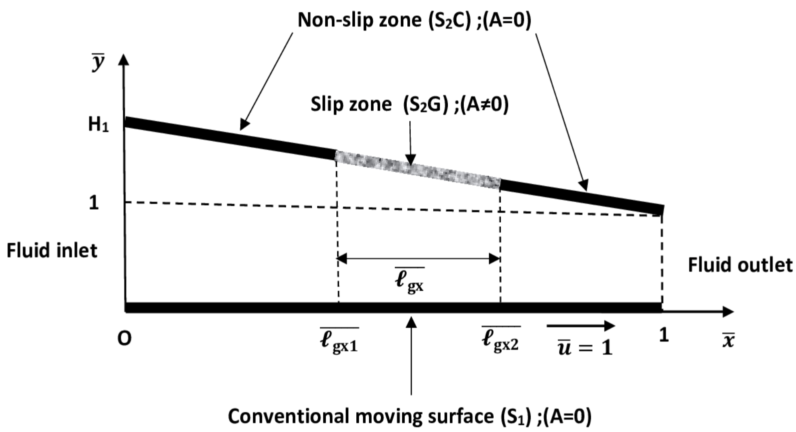

Fig. 6. One-dimensional schematic of a pad bearing.

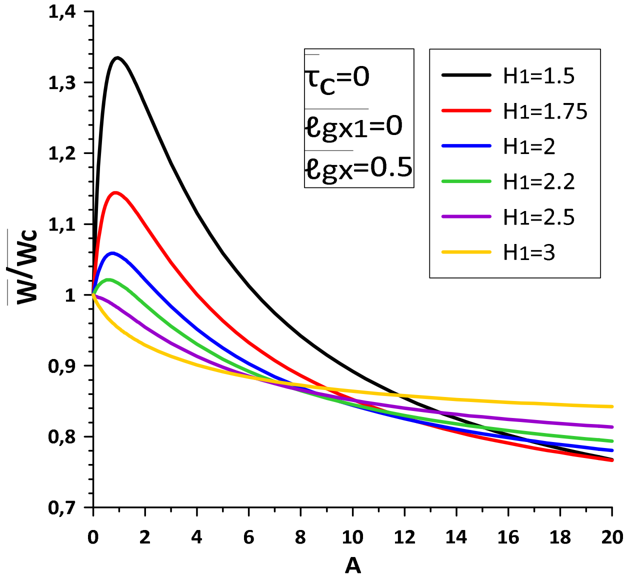

Fig. 7. Load capacity gain as a function of the dimensionless slip coefficient.

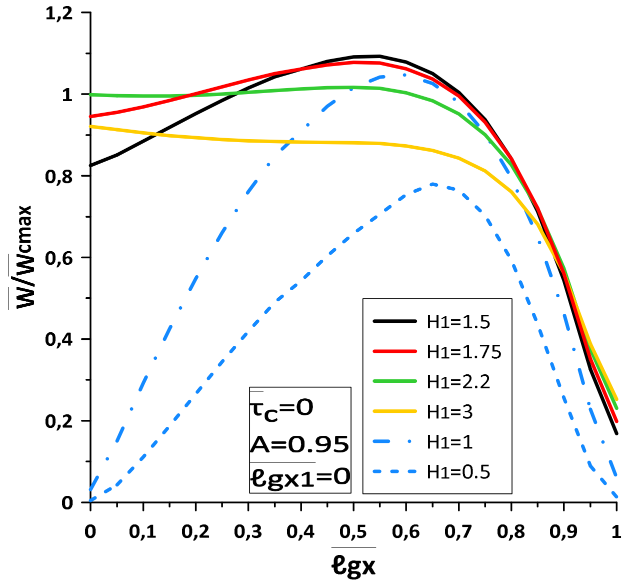

Fig. 8. Optimum load capacity gain as a function of the slip zone length.

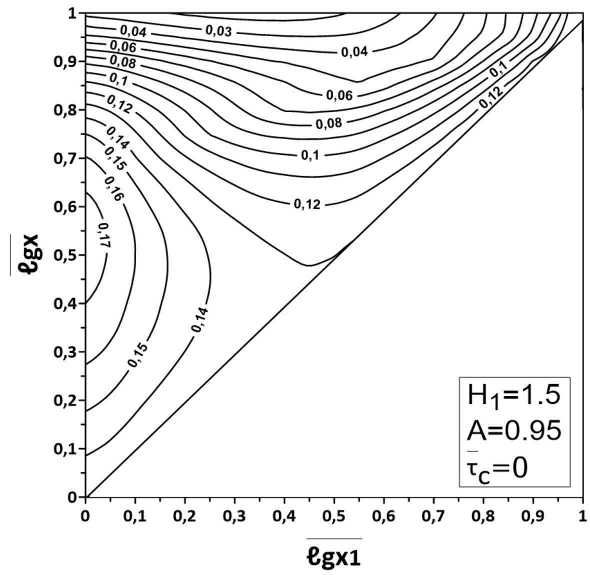

Fig. 9. Dimensionless load capacity as a function of the position and the extent of the slip zone.

In Fig. 9, isovalues of dimensionless load capacity ($\overline{W}$) are plotted against the slip zone extent ($\overline{\ell}_{gx}$) and position ($\overline{\ell}_{gx1}$) on the pad bearing's fixed surface. This is for a convergence ratio ($H_1 = 1.5$) and a dimensionless slip coefficient ($A = 0.95$).

It is revealed that the maximum load capacity is achieved when the slip zone begins at the entry of the contact ($\overline{\ell}_{gx1} = 0$) and extends to ($\overline{\ell}_{gx} = 55\%$). The maximum dimensionless load capacity in this case is (0.175). Conversely, for a starting position of the slip zone ($\overline{\ell}_{gx1}$) greater than or equal to (0.25), it is noted that the load capacity decreases with the slip zone extent.

This result is consistent with those of Zhang et al. [26] and Zhang and Zhu [27]. Indeed, these authors show using optimization methods (Genetic Algorithm and Monte Carlo method) that the optimal slip zone, which maximizes load capacity and minimizes friction force, always starts at the contact entry and has a length that exceeds half of the contact length.

Figure 10 depicts the evolution of the dimensionless pressure field $\overline{P}(\overline{x})$ for a dimensionless slip coefficient ($A = 0.95$) and a slip zone length of (55%). This is done for convergence ratios (H_1) ranging from (1.5) to (3).

It is observed that introducing the slip condition results in both a discontinuity and a change in the pressure field distribution. The profile of this field is triangular when the convergence ratio is (1.5) and becomes parabolic as this ratio increases. Additionally, the maximum dimensionless pressure value corresponds to the pad bearing with a convergence ratio ($H_1 = 1.5$), reaching (0.310), which exceeds the maximum pressure of the conventional pad bearing by (19%).

For an infinitely long pad bearing having zero critical shear stress ($\overline{\tau}_c = 0$), Wu et al. [15] obtained a similar evolution of the dimensionless pressure field across various convergence ratios (H_1). According to their results, a convergence ratio ($H_1 \approx 0.9$) (almost parallel surfaces) and a slip length starting at the contact entry and equal to (65%) are optimal values for the pad bearing. The maximum dimensionless pressure in the film in this case is (0.650).

When the slip zone length ($\overline{\ell}_{gx}$) is equal to (55%), Fig. 11 illustrates the evolution of the dimensionless friction force ratio ($\overline{F}_x / \overline{F}_{xc}$) in the x-direction, relative to that of a conventional pad bearing for the same convergence ratio, plotted against the dimensionless slip coefficient (A). This is done for convergence ratios (H_1) ranging from (1.5) to (3).

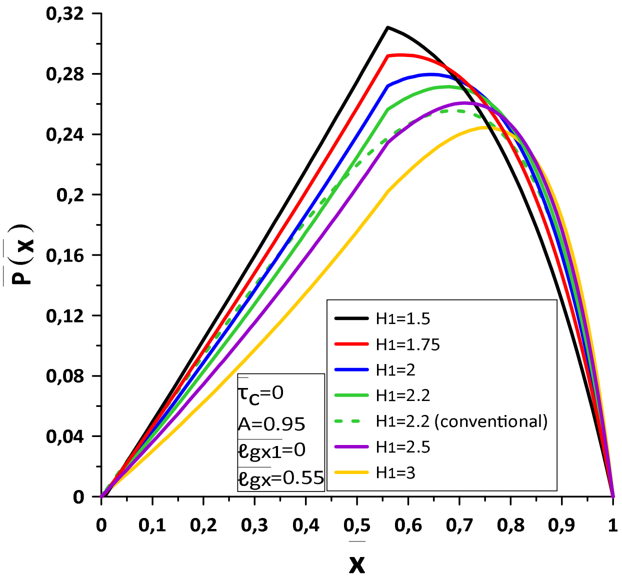

Fig. 10. Evolution of the dimensionless pressure field in the film.

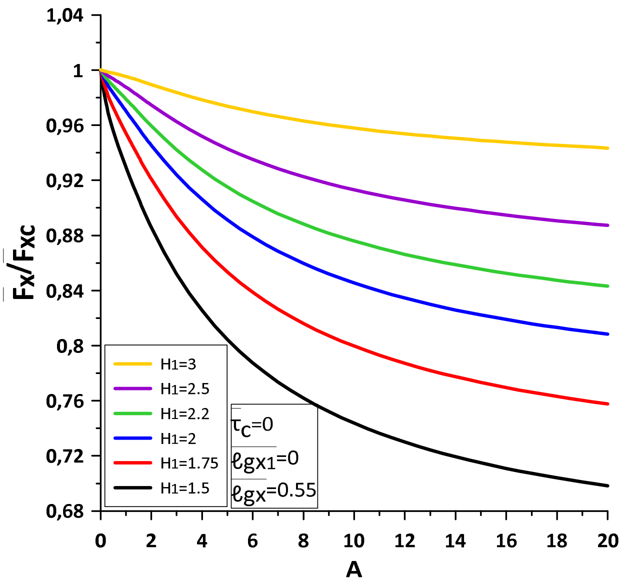

Fig. 11. Dimensionless friction force ratio in the x-direction as a function of the dimensionless slip coefficient.

Firstly, it is noted that the friction force decreases relative to that of the conventional pad bearing as the slip coefficient increases, across all convergence ratios (H_1). This reduction is more pronounced for a ratio of (H_1 = 1.5), which yields a dimensionless friction force value ($\bar{F}_x$ = 0.589) for a slip coefficient (A = 20), resulting in a friction force gain (i.e, minimum friction) of (-30%) compared to the conventional pad bearing with the same convergence ratio. It should be noted that this gain in terms of friction comes at the expense of load capacity, which is only (80%) in this case (see Fig. 7). Secondly, it is observed that for an identical slip coefficient, the friction force gain (i.e., minimum friction) relative to the conventional pad bearing decreases as the convergence ratio increases.

The conflict between the gain in load capacity and the gain in friction force, which necessarily requires a trade-off, is generally addressed using optimization methods. In the case of a multi-objective optimization involving the maximization of load capacity and simultaneous minimization of friction force, Zhang and Zhu [27] demonstrate that by minimizing (by varying a weighting factor) a fictitious function expressed as a linear combination of load capacity and friction force, one can obtain a trade-off curve that is very useful when seeking to balance different objectives.

In Fig. 12, the evolution of the dimensionless volumetric flow rate ratio ($\bar{Q}_x / \bar{Q}_{xc}$) in the x-direction is shown, relative to that of a conventional pad bearing for the same convergence ratio, as a function of the dimensionless slip coefficient (A). This is for a slip zone length ($\bar{\ell}_{gx}$) of (55%) and convergence ratios (H_1) of (1.5) to (3). The flow rate is calculated at the entry of the contact.

On the one hand, it is noted that for any convergence ratio (H_1) between (1.5) and (2.5), the flow rate ratio increases until it reaches a maximum value, which corresponds to a dimensionless slip coefficient (A) value close to (1), after which it decreases monotonically. On the other hand, results show that above a dimensionless slip coefficient (A) value close to (9.5), the non-conventional pad bearing provides a minimal volumetric flow rate compared to that of a conventional pad bearing with the same convergence ratio. Convergence ratio values of (2.5) and (3) result in a minimal flow rate for the non-conventional pad bearing, regardless of the slip coefficient value. Besides, regarding convergence ratios (H_1) ranging from (1.5) to (2.2), the conventional pad bearing provides the minimum volumetric flow rate until a critical value of the dimensionless slip coefficient is reached, which depends on the convergence ratio. Finally, it is important to recognize that any significant load capacity gain inevitably comes with an increase in volumetric flow rate. Specifically, a non-zero velocity field at the Fluid/Surface (S_2G) interface will inevitably lead to an intensification and a change in the velocity profile at a given section, and consequently affect its flow rate.

4.2. Non-zero critical shear stress case ($\bar{\tau}_c \neq 0$)

For a range of dimensionless critical shear stress quantities, Fig. 13 depicts the evolution of the dimensionless load capacity ($\bar{W}$) plotted against the convergence ratio (H_1). This is for a dimensionless slip coefficient (A = 0.95) and a slip zone length of (55%).

Firstly, it is observed that for any critical shear stress value, the load capacity rises until it attains a maximum value, which depends on the convergence ratio (H_1). Secondly, it is noted that the pad bearing can sustain a load even when it is divergent (H_1 < 1) or has parallel surfaces (H_1 = 1). However, for a critical shear stress set at (1), the load capacity is zero when the pad bearing is divergent or has parallel surfaces. Furthermore, the maximum dimensionless load capacity is attained for a zero dimensionless critical shear stress ($\bar{\tau}_c$ =0) and a convergence ratio (H_1 = 1.5). In this case, the maximum load capacity reaches (0.175). Finally, it is noted that for convergence ratios (H_1 > 2.2), the dimensionless critical shear stress has almost no impact on the load capacity.

This trend regarding the evolution of dimensionless load capacity plotted against the convergence ratio and for various values of critical shear stress agrees with the results of Wu et al. [15]. Nevertheless, for a critical shear stress value of (1), the pad bearing's load capacity is non-zero when it is divergent or has parallel surfaces.

With a convergence ratio (H_1 = 1.5), dimensionless slip coefficient (A = 0.95), and a slip zone length ($\bar{\ell}_{gx}$) of (55%), Fig. 14 illustrates the evolution of dimensionless velocity fields $\bar{u}(\bar{y})$ at various sections of the contact (Table 3). This is for two dimensionless critical shear stress values; ($\bar{\tau}_c$ = 0, case a) and ($\bar{\tau}_c$ = 0.5, case b). The start of the slip zone is assumed to be at the entry of the contact ($\bar{\ell}_{gx1} = 0$) in both cases. In each case, these velocity field profiles (red curves) are compared to those (blue curves) obtained assuming a conventional pad bearing.

Table 3 presents the slip velocities at various points on the Fluid/Surface (S_2) interface. These points labeled A, B, C, D, and E, correspond to different sections of the contact. Points A, B, and C represent the Fluid/Surface (S_2G) interface, while points D and E represent the Fluid/Surface (S_2C) interface.

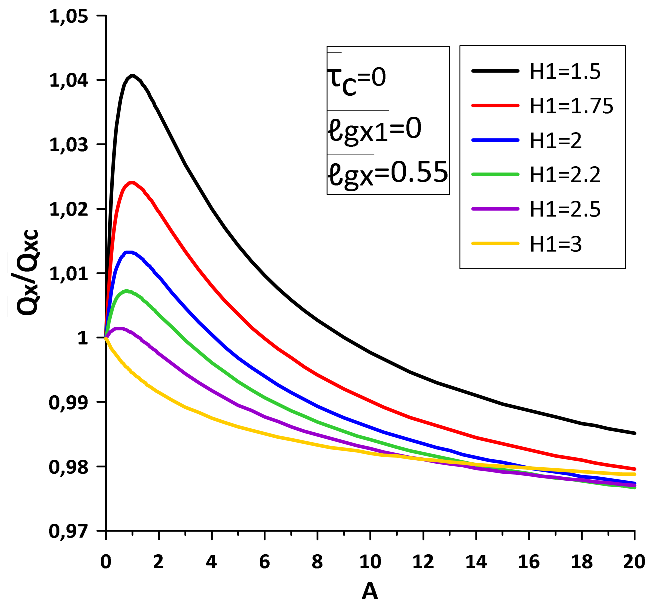

Fig. 12. Dimensionless flow rate ratio in the x-direction as a function of the dimensionless slip coefficient.

Table 3. Values of velocities at the upper wall interface.

		Case a	Case b
		$\overline{\tau}_c = 0$	$\overline{\tau}_c = 0.5$
Point	Section $\overline{x}$	$\overline{u}(\overline{y} = H)$	$\overline{u}(\overline{y} = H)$
A	0.15	0.1122	0
B	0.3	0.1267	0.0081
C	0.55	0.1536	0.0467
D	0.7	0	0
E	0.85	0	0

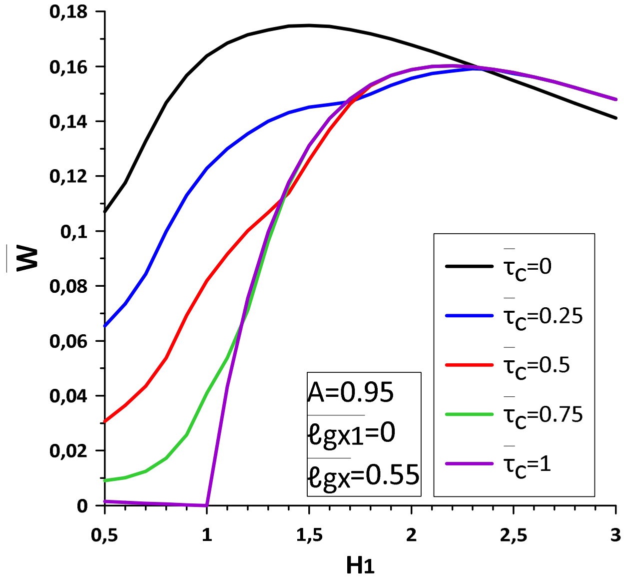

Fig. 13. Dimensionless load capacity as a function of the convergence ratio.

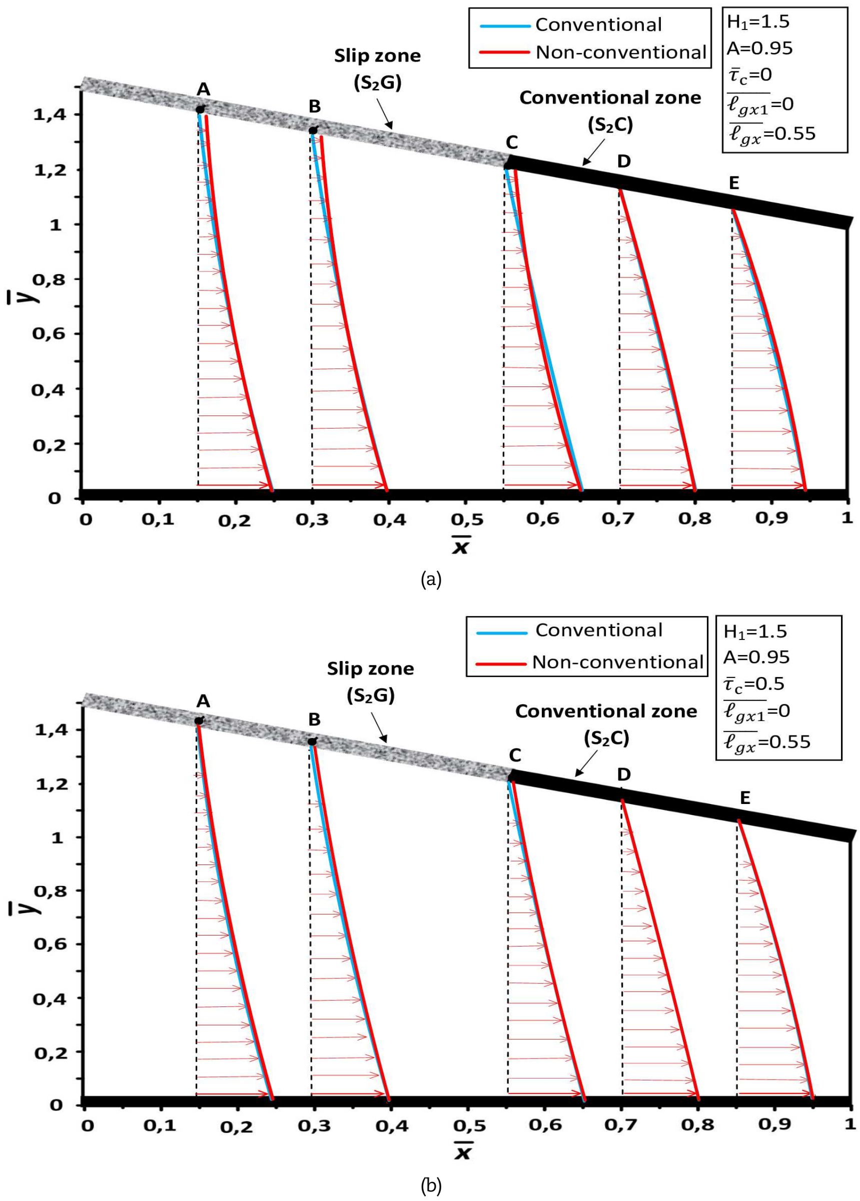

Fig. 14. Profiles of dimensionless fluid velocity fields $\overline{u}(\overline{y})$.

From one perspective, results show an increase in the slip velocity from the entry of the contact to the slip zone end (S_2G), regardless of the critical shear stress. From another perspective, a rise in the critical shear stress results in a reduction in the slip velocity at points A, B, and C. At points D and E within the conventional zone (S_2C), the fluid velocity at the wall is zero everywhere (wall adhesion). Moreover, for a zero critical shear stress ($\overline{\tau}_c = 0$), the maximum slip velocity is observed at interface C, which corresponds to the end of the slip zone, reaching approximately (15.36%) of the velocity (U). Increasing the critical shear stress ($\overline{\tau}_c = 0.5$) results in a decrease in this slip velocity to (4.67%) at the same interface.

In summary, the findings from this numerical investigation reveal the critical connections between load capacity, pressure distribution, and friction force in the pad bearing under varying conditions. The results indicate that optimal load capacity gain is achieved at a specific convergence ratio ($H_1 = 1.5$) and slip coefficient ($A = 0.95$). Furthermore, the optimal pressure distribution occurs under the same conditions while the friction force decreases with a different slip coefficient ($A = 20$). This trade-off between load capacity and friction force underscores the need for careful optimization in slip zone design. More than that, the slip zone length and its starting position play crucial roles in determining the hydrodynamic performances of pad bearings. The ability of non-conventional pad bearings to support loads under divergent or parallel surfaces further differentiates them from traditional pad bearings.

5. Conclusion

The hydrodynamic behavior of a one-dimensional pad bearing, with its upper surface partially or fully subjected to the slip boundary condition, has been numerically determined by solving the modified Reynolds equation. Considering the Navier slip condition significantly affects the performance of the pad bearing, particularly with zero critical shear stress. The slip zone position and extent of the slip zone have a non-negligible influence on the pressure distribution within the contact area. Dimensionless slip coefficients (A) within the range [0,3] strongly affect the pad bearing's load capacity values, especially for convergence ratios (H_1) ranging from (1.5) to (2.2). For a convergence ratio ($H_1 = 1.5$) and a half non-conventional upper surface (slip zone length of 55%), the non-conventional pad bearing exhibits a potential load capacity increase of around (33.5%) compared to a conventional pad bearing with the same convergence ratio, and (9.3%) compared to the optimal pad bearing ($H_1 = 2.2$), and it provides a relative gain in terms of friction force minimization compared to a conventional pad bearing, which can reach up to (-30%). The ability of the non-conventional pad bearing to support loads under divergent or parallel surfaces distinguishes it from conventional pad bearings, which cannot achieve this under such conditions. These improvements make this non-conventional pad bearing suitable for various industrial applications that operate at rotational systems, including turbomachinery and automotive systems where increased load capacity and reduced friction are critical. Future research should focus on extending this study to two dimensions. Additionally, it is believed that an optimization approach should complement this study to ensure that the gain in load capacity does not come at the expense of friction force or flow rate.

Author Contributions

I. Messoude developed the mathematical modeling, conducted the simulations, and prepared all the figures under the co-author's guidance, S. Aghzer. The manuscript was written through the contribution of all authors. All authors discussed the results, reviewed, and approved the final version of the manuscript.

Acknowledgments

Not applicable.

Conflict of Interest

The authors declared no potential conflicts of interest concerning the research, authorship, and publication of this article.

Funding

The authors received no financial support for the research, authorship, and publication of this article.

Data Availability Statements

Not applicable.

Nomenclature

$A = \alpha\mu/h_{2x}$	Dimensionless slip coefficient
b	Slip length [m]
F_x	Dimensional friction force in the x-direction [N]
$\overline{F}_x = [h_{2x}/\mu U \ell_x \ell_z] F_x$	Dimensionless friction force in the x-direction
F_{xc}	Dimensional friction force in the x-direction of a conventional pad bearing [N]
$\overline{F}_{xc} = [h_{2x}/\mu U \ell_x \ell_z] F_{xc}$	Dimensionless friction force in the x-direction of a conventional pad bearing
F_z	Dimensional friction force in the z-direction [N]
$\overline{F}_z = [h_{2x}/\mu U \ell_x \ell_z] F_z$	Dimensionless friction force in the z-direction
$h(x,z)$	Dimensional film thickness field [m]
$H(\bar{x},\bar{z}) = h(x,z)/h_{2x}$	Dimensionless film thickness field
h_1	Dimensional film thickness at the contact inlet [m]
Q_x	Dimensional fluid volumetric flow rate in the x-direction [m³/s]
$\overline{Q}_x = Q_x/U h_{2x} \ell_z$	Dimensionless fluid volumetric flow rate in the x-direction
Q_{xc}	Dimensional fluid volumetric flow rate in the x-direction of a conventional pad bearing [m³/s]
$\overline{Q}_{xc} = Q_{xc}/U h_{2x} \ell_z$	Dimensionless fluid volumetric flow rate in the x-direction of a conventional pad bearing
Q_z	Dimensional fluid volumetric flow rate in the z-direction [m³/s]
$\overline{Q}_z = Q_z/U h_{2x} \ell_x$	Dimensionless fluid volumetric flow rate in the z-direction
S_1	Lower contact surface (moving)
S_2	Upper contact surface (fixed)
U	Translation velocity of the lower surface (S1) [m/s]
$u(y)$	Dimensional velocity field in the x-direction [m/s]
$\bar{u}(\bar{y}) = u(y)/U$	Dimensionless velocity field in the x-direction

h_{2x}	Dimensional film thickness at the contact outlet in the x-direction [m]
$H_1 = h_1/h_{2x}$	Convergence ratio in the x-direction
h_{2z}	Dimensional film thickness at the contact outlet in the z-direction [m]
i_{gx1}	Index of the start of the slip zone in the x-direction
i_{gx2}	Index of the end of the slip zone in the x-direction
i_{gz1}	Index of the start of the slip zone in the z-direction
i_{gz2}	Index of the end of the slip zone in the z-direction
$\ell_{gx} = \ell_{gx2} - \ell_{gx1}$	Dimensional slip zone length in the x-direction [m]
$\overline{\ell_{gx}} = \overline{\ell_{gx2}} - \overline{\ell_{gx1}}$	Dimensionless slip zone length in the x-direction
ℓ_{gx1}	Dimensional x-coordinate at the start of the slip zone [m]
$\overline{\ell_{gx1}} = \ell_{gx1}/\ell_x$	Dimensionless x-coordinate at the start of the slip zone
ℓ_{gx2}	Dimensional x-coordinate at the end of the slip zone [m]
$\overline{\ell_{gx2}} = \ell_{gx2}/\ell_x$	Dimensionless x-coordinate at the end of the slip zone
$\ell_{gz} = \ell_{gz2} - \ell_{gz1}$	Dimensional slip zone length in the z-direction [m]
$\overline{\ell_{gz}} = \overline{\ell_{gz2}} - \overline{\ell_{gz1}}$	Dimensionless slip zone length in the z-direction
ℓ_{gz1}	Dimensional z-coordinate at the start of the slip zone [m]
$\overline{\ell_{gz1}} = \ell_{gz1}/\ell_z$	Dimensionless z-coordinate at the start of the slip zone
ℓ_{gz2}	Dimensional z-coordinate at the end of the slip zone [m]
$\overline{\ell_{gz2}} = \ell_{gz2}/\ell_z$	Dimensionless z-coordinate at the end of the slip zone
ℓ_x	Contact length in the x-direction [m]
ℓ_z	Contact width in the z-direction [m]
$L = \ell_x/\ell_z$	Aspect ratio
M	Number of x-direction discretization points
N	Number z-direction of discretization points
$P(x,z)$	Dimensional pressure field in the film [Pa]
$\bar{P}(x,z) = [h_{2x}^2/\mu U \ell_x] P(x,z)$	Dimensionless pressure field in the film
$\bar{P}_{cmax}$	Dimensionless maximum pressure in a conventional pad bearing ($\bar{P}_{cmax} = 0.260$ for $H_1 = 2.2$; [1])
u_p	Dimensional wall velocity in the x-direction [m/s]
W	Dimensional load capacity [N]
$\overline{W} = [h_{2x}^2/\mu U \ell_x^2 \ell_z] W$	Dimensionless load capacity
W_c	Dimensional load capacity of a conventional pad bearing [N]
$\overline{W_c} = [h_{2x}^2/\mu U \ell_x^2 \ell_z] W_c$	Dimensionless load capacity of a conventional pad bearing
$\overline{W}_{cmax}$	Dimensionless maximum load capacity of a conventional pad bearing ($\overline{W}_{cmax} = 0.160$ for $H_1 = 2.2$; [1])
$w(y)$	Dimensional velocity field in the z-direction [m/s]
$\overline{w}(\bar{y}) = w(y)/U$	Dimensionless velocity field in the z-direction
x	Dimensional coordinate in the x-direction [m]
$\bar{x} = x/\ell_x$	Dimensionless coordinate in the x-direction
y	Dimensional coordinate in the y-direction [m]
$\bar{y} = y/h_{2x}$	Dimensionless coordinate in the y-direction
z	Dimensional coordinate in the z-direction [m]
$\bar{z} = z/\ell_z$	Dimensionless coordinate in the z-direction
α	Dimensional slip coefficient [m/Pa.s]
$\Delta\bar{x}$	Grid spacing in the x-direction
$\Delta\bar{z}$	Grid spacing in the z-direction
ε_p	Pressure field calculation accuracy
μ	Dynamic fluid viscosity [Pa.s]
σ	Over-relaxation coefficient
τ_c	Dimensional critical shear stress [Pa]
$\bar{\tau}_c = \tau_c\, h_{2x}/\mu U$	Dimensionless critical shear stress
τ_p	Dimensional wall shear stress [Pa]
τ_{xy}	Dimensional shear stress in the fluid in the x-direction [Pa]
τ_{yz}	Dimensional shear stress in the fluid in the z-direction [Pa]
Ω	Discretization domain

Appendix A

The rectangular domain $(\Omega = \ell_x * \ell_z)$ of the surface (S_1) defined as:

$$0 \le \bar{x} \le 1$$
$$0 \le \bar{z} \le 1 \tag{A.1}$$

is discretized into (M*N) elementary rectangles of surface $(\Delta\bar{x} * \Delta\bar{z})$. Each node P(i,j) is identified by its discrete coordinates (i,j), which replace the continuous variables $(\bar{x}, \bar{z})$. (Fig. A1).

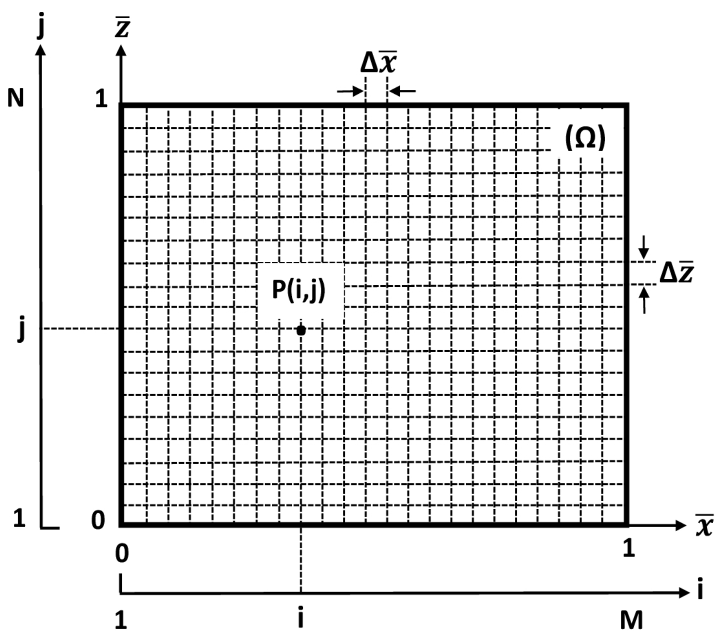

Fig. A1. Numerical grid.

The boundary conditions on the pressure field of Eq. (12) are expressed as:

$$\begin{aligned}\bar{P}(i,1) &= \bar{P}(i,N) = 0; \quad i = 1,M \\ \bar{P}(1,j) &= \bar{P}(M,j) = 0; \quad j = 1,N\end{aligned} \tag{A.2}$$

For a function $g(\bar{x},\bar{z})$, the first and second order partial derivatives at the point P(i,j) can be expressed as:

$$\begin{aligned}\frac{\partial g}{\partial \bar{x}}(i,j) &= \frac{g(i+1,j)-g(i-1,j)}{2\Delta\bar{x}} \\ \frac{\partial^2 g}{\partial \bar{x}^2}(i,j) &= \frac{g(i+1,j)+g(i-1,j)-2g(i,j)}{(\Delta\bar{x})^2} \\ \frac{\partial g}{\partial \bar{z}}(i,j) &= \frac{g(i,j+1)-g(i,j-1)}{2\Delta\bar{z}} \\ \frac{\partial^2 g}{\partial \bar{z}^2}(i,j) &= \frac{g(i,j+1)+g(i,j-1)-2g(i,j)}{(\Delta\bar{z})^2}\end{aligned} \tag{A.3}$$

By substituting these expressions into Eq. (11), the expression for the pressure at a node (i,j) can ultimately be written as:

$$\bar{P}(i,j) = T_A(i,j)\bar{P}(i-1,j) + T_B(i,j)\bar{P}(i+1,j) + T_C(i,j)\bar{P}(i,j-1) + T_D(i,j)\bar{P}(i,j+1) + T_E(i,j) \qquad i = 2,M-1, \quad j = 2,N-1 \tag{A.4}$$

In this expression, T_A, T_B, T_C, T_D, and T_E which represent the pressure coefficients near the node (i,j), are written as:

$$\begin{aligned}&T_A(i,j) = \left[\frac{K_3}{(\Delta\bar{x})^2} - \frac{K_1}{2\Delta\bar{x}}\right]/DEN; \qquad T_D(i,j) = \left[\frac{K_4}{(\Delta\bar{z})^2} + \frac{K_2}{2\Delta\bar{z}}\right]/DEN \\ &T_B(i,j) = \left[\frac{K_3}{(\Delta\bar{x})^2} + \frac{K_1}{2\Delta\bar{x}}\right]/DEN; \qquad T_E(i,j) = (K_5+K_6+K_7+K_8)/DEN \\ &T_C(i,j) = \left[\frac{K_4}{(\Delta\bar{z})^2} - \frac{K_2}{2\Delta\bar{z}}\right]/DEN; \qquad i = 2,M-1,\ j = 2,N-1\end{aligned} \tag{A.5}$$

In these expressions, the terms (K_1 to K_8) depend on the film thickness field H(i,j) and the slip field A(i,j), as well as their first-order derivatives.

With:

$$DEN = 2\left[\frac{K_3}{(\Delta\bar{x})^2} + \frac{K_4}{(\Delta\bar{z})^2}\right] \tag{A.6}$$

$$\begin{aligned}&K_1 = \frac{3H}{(H+A)}\left[(H+A)^2 + A^2\right]\frac{\partial H}{\partial \bar{x}} + \frac{3H^3}{(H+A)}\frac{\partial A}{\partial \bar{x}}; \qquad K_5 = \frac{-6H(1+A\bar{\tau}_c)}{(H+A)}\frac{\partial H}{\partial \bar{x}} \\ &K_2 = L^2\left[\frac{3H}{(H+A)}\left[(H+A)^2 + A^2\right]\frac{\partial H}{\partial \bar{z}} + \frac{3H^3}{(H+A)}\frac{\partial A}{\partial \bar{z}}\right]; \qquad K_6 = \frac{-6LA\bar{\tau}_c H}{(H+A)}\frac{\partial H}{\partial \bar{z}} \\ &K_3 = H^2(H+4A); \qquad K_7 = \frac{6H(\bar{\tau}_c H - 1)}{(H+A)}\frac{\partial A}{\partial \bar{x}} \\ &K_4 = L^2H^2(H+4A); \qquad K_8 = \frac{6L\bar{\tau}_c H^2}{(H+A)}\frac{\partial A}{\partial \bar{z}}\end{aligned} \tag{A.7}$$

The system of linear equations Eq. (A.4) is solved, taking into account the boundary conditions on the pressure Eq. (A.2), using the iterative Gauss-Seidel method with an over-relaxation coefficient (σ) such that:

$$\bar{P}(i,j) = (1-\sigma)\bar{P}(i,j) + \sigma\left[T_A(i,j)\bar{P}(i-1,j) + T_B(i,j)\bar{P}(i+1,j) + T_C(i,j)\bar{P}(i,j-1) + T_D(i,j)\bar{P}(i,j+1) + T_E(i,j)\right], \quad i = 2,M-1,\ j = 2,N-1 \tag{A.8}$$

The over-relaxation coefficient (σ), which must be strictly greater than (1), should be chosen optimally to accelerate the convergence of the calculation process. In most hydrodynamic lubrication problems, this coefficient typically ranges between (1.5) and (1.85) [1]. In this case, the chosen value is $(\sigma) = 1.6$.

References

[1] Frene, J., Nicolas, D., Degueurce, B., Berthe, D., Godet, M., *Lubrification hydrodynamique. Paliers et Butées*, Collection des Etudes et Recherche d'Electricité de France, Eyrolles, 1990.

[2] Liravi, M., Pakzad, H., Moosavi, A., Nouri-Borujerdi, A., A comprehensive review on recent advances in superhydrophobic surfaces and their applications for drag reduction, *Progress in Organic Coatings*, 140, 2020, 105537.

[3] Navier, C., *Mémoire sur les lois du mouvement des fluides*, Mémoires de l'Académie Royale des Sciences de l'Institut de France, 1822.

[4] Maxwell, J.C., On stresses in rarified gases arising from inequalities of temperature, *Philosophical Transactions of the Royal Society of London*, 170, 1879, 231-256.

[5] Thompson, P.A., Troian, S.M., A general boundary condition for liquid flow at solid surfaces, *Nature*, 389(6649), 1997, 360-362.

[6] Tabeling, P., Phénomènes de glissement à l'interface liquide-solide, *Comptes Rendus Physique*, 5(5), 2004, 531–537.

[7] Vinogradova, O.I., Slippage of water over hydrophobic surfaces, *International Journal of Mineral Processing*, 56(1-4), 1999, 31-60.

[8] Charlaix, E., Cottin-Bizonne, C., Crassoux, J., Leroy, S., Restagno, F., Steingerger, A., Propriétés hydrodynamiques au voisinage d'une surface, *Reflets de la physique*, 22, 2011, 14-18.

[9] Sochi, T., Slip at Fluid-Solid Interface, *Polymer Reviews*, 51, 2011, 309-340.

[10] Pit, R., Hervet, H., Léger, L., Friction and slip of a simple liquid at a solid surface, *Tribology Letters*, 7, 1999, 147-152.
[11] Henry, C.L., Craig, V.S.J., Measurement of no-slip and slip boundary conditions in confined Newtonian fluids using atomic force microscopy, *Physical Chemistry Chemical Physics*, 11(41), 2009, 9514-9521.
[12] Spikes, H., Granick, S., Equation for slip of simple liquids at smooth solid surfaces, *Langmuir*, 19(12), 2003, 5065-5071.
[13] Spikes, H.A., The half-wetted bearing. Part 1: extended Reynolds equation, *Proceedings of the Institution of Mechanical Engineers, Part J: Journal of Engineering Tribology*, 217(1), 2003, 1-14.
[14] Salant, R.F., Fortier, A.E., Numerical analysis of a slider bearing with a heterogeneous slip/no-slip surface, *Tribology Transactions*, 47(3), 2004, 328-334.
[15] Wu, C.W., Ma, G.J., Zhou, P., Low friction and high load support capacity of slider bearing with a mixed slip surface, *Journal of Tribology*, 128, 2006, 904-907.
[16] Wu, C., Performance of hydrodynamic lubrication journal bearing with a slippage surface, *Industrial Lubrication and Tribology*, 60(6), 2008, 293-298.
[17] Rao, T.V.V.L.N., Analysis of single-grooved slider and journal bearing with partial slip surface, *Journal of Tribology*, 132(1), 2010, 014501.
[18] Lin, Q., Wei, Z., Tang, Y., Numerical study on shear flow in sliding bearing with partial slip surface, *45th CIRP Conference on Manufacturing Systems*, Athens, Greece, 197-202, 2012.
[19] Tauviqirrahman, M., Ismail, R., Jamari, J., Schipper, D.J., Friction reduction in lubricated-MEMS with complex slip surface pattern, *The Malaysian International Tribology Conference*, Kuala Lumpur, Malaysia, 331-337, 2013.
[20] Tauviqirrahman, M., Ismail, R., Schipper, D.J., Optimization of the complex slip surface and its effect on the hydrodynamic performance of two-dimensional lubricated contacts, *Computers & Fluids*, 79, 2013, 27–43.
[21] Zidane, I., Zahloul, H., Hajjam, M., Abbadeni, M., Modeling and analysis of the slip conditions in hydrodynamic lubrication, *Arabian Journal for Science and Engineering*, 39, 2014, 7199-7210.
[22] Guo, L., Wong, P.L., Guo, F., Effects of viscosity and sliding speed on boundary slippage in thin film hydrodynamic lubrication, *Tribology International*, 107, 2017, 85-93.
[23] Sun, B.W., Chen, L., Guo, L., Wang, W., Wong, P.L., Experimental Evidence on the Enhancement of Bearing Load Capacity by Localised Boundary Slip Effect, *Tribology Letters*, 69, 2021, 1-8.
[24] Xie, Z.L., Ta, N., Rao, Z.S., The lubrication performance of water lubricated bearing with consideration of wall slip and inertial force, *Journal of Hydrodynamics, Ser. B*, 29(1), 2017, 52-60.
[25] Çam, M.Y., Giacopini, M., Dini, D., Biancofiore, L., A numerical algorithm to model wall slip and cavitation in two-dimensional hydrodynamically lubricated contacts, *Tribology International*, 184, 2023, 108444.
[26] Zhang, H., Liu, Y., Dai, S., Li, F., Dong, G., Optimization of boundary slip region on bearing sliders to improve tribological performance, *Tribology International*, 168, 2022, 107446.
[27] Zhang, W., Zhu, B., Optimization design for slip/no-slip configuration of hydrophobic sliding bearings using Monte Carlosearch, *Tribology International*, 178, 2023, 1080340.
[28] Dadouche, A., *Etude des phénomènes thermiques dans les butées hydrodynamiques*, Thèse de Doctorat de l'Université de Poitiers, 1998.

ORCID iD

Ihssane Messoude https://orcid.org/0009-0002-1576-4487
Samir Aghzer https://orcid.org/0009-0000-8384-2243

How to cite this article: Messoude I., Aghzer S. Numerical study of the effects of the Navier slip boundary condition on the hydrodynamic performances of a Newtonian fluid-lubricated pad bearing, *J. Appl. Comput. Mech.*, 11(3), 2025, 754-769. https://doi.org/10.22055/jacm.2024.47772.4788